

Hartnady, M.I.H., et al., 2023, Origin of Archean Pb isotope variability through open-system Paleoarchean crustal anatexis: *Geology*, <https://doi.org/10.1130/G51507.1>

Supplemental Material

Analytical details and Pb isotope data tables

Origin of Archean Pb isotope variability through open-system Paleoarchean crustal anatexis

MIH. Hartnady¹, CL Kirkand¹, SP Johnson² RH Smithies^{1,2}, LS Doucet^{3,4}, and DR Mole⁵

¹Timescales of Mineral Systems Group, School of Earth and Planetary Science, Curtin University, Perth, Western Australia

²Geological Survey of Western Australia, 101 Plain Street, East Perth, Western Australia.

³ Earth Dynamics Research Group, School of Earth and Planetary Science, Curtin University, Perth, Western Australia

⁴ State Key Laboratory of Geological Processes and Mineral Resources, China University of Geosciences, Wuhan, Hubei, 430074, China.

⁵ Geoscience Australia, GPO Box 378, Canberra, ACT 2601, Australia

Tables of Contents:

Materials and Methods

LA-ICP-MS Analyses

Data Compilation

Two-stage Pb Isotope Source Model Age Calculations

Spatial Mapping Methods

Pb Isotope Evolution Modelling

Supplementary Tables

Table DR1: Summary of Pb isotope results for NIST612 glass for all analytical sessions.

Table DR2: Parameters used for Pb isotope modelling.

Supplementary Figures

Figure DR1: Interpolated maps of whole-rock Nd isotope two-stage depleted mantle model ages, showing the spatial variation in age of the crust across the Yilgarn Craton

Figure DR2: Linear Pb isotope evolution diagrams showing Pb isotope composition of granites from the Yilgarn Craton and various Pb isotope evolution model models.

Figure DR3: Pb isotope evolution diagrams showing the initial Pb isotope compositions of granites and ores from the Yilgarn Craton along with different modelled Pb isotope evolution curves.

Methods

LA-ICP-MS Analyses:

Light fractions from mineral separation of a regional geochronology program in granites, previously dated by zircon U-Th-Pb using secondary ion mass spectrometry (SIMS), were mounted in 25mm epoxy rounds and polished to expose the grain interiors. A Tescan TIMA automated quantitative petrological analyzer was used to characterize the sample material. The characterization procedure involved back-scattered electron (BSE) imaging at 1 μm resolution followed by energy dispersive X-ray spectroscopy (EDX) dot mapping with 9 μm spacing. This characterization process was used to identify orthoclase grains suitable for isotopic analysis and locate areas of grains that were altered, contain cracks and/or inclusions, particularly those likely to host U and Th (e.g. zircon, apatite etc.). The Pb isotopic composition of orthoclase crystals were determined by laser-ablation inductively coupled plasma mass spectrometry (LA-ICPMS) at the GeoHisotry Facility in the John de Laeter Centre at Curtin University. Data were acquired over 22 analytical sessions between June of 2020 and November of 2022. Analyses were carried out on a Nu Plasma II (NPII) multi-collector mass spectrometer used in conjunction with a Resonetics S-155-LR 193 nm excimer laser ablation system. Initially, isotopes of interest were measured using a combination of Faraday cups (^{208}Pb , ^{207}Pb , ^{206}Pb) and ion counters ($^{204}\text{Pb} + \text{Hg}$, ^{202}Hg , ^{200}Hg , ^{198}Hg) with 0.8 s integration time for all masses. In early 2022 an additional ion counter was added to the collector array allowing all isotopes of interest to be measured on ion counters (^{238}U , ^{208}Pb , ^{207}Pb , ^{206}Pb , $^{204}\text{Pb} + \text{Hg}$, and ^{202}Hg),

Analyses using faraday cups were carried out using a circular spot of 50 μm diameter with a laser fluence between 2.2-2.5 $\text{J}\cdot\text{cm}^{-2}$, as measured at the sample surface, and a pulse frequency of 10 Hz. The spot size was reduced to 33 μm after the change in detector configuration owing to the increased sensitivity of the ion counter, except for session 16 which used a 16 μm spot size. In both cases, data acquisition consisted of two cleaning pulses, 20 s blank flush out, 40 s of baseline collection, 30 s ablation followed by 15 s of additional baseline correction. The sample cell was flushed with ultrahigh purity He (350 mL/min) and N_2 (1.0 mL/min) and high purity Ar was employed as the plasma carrier gas. The isobaric interference of ^{204}Hg on the 204 ion beam was corrected using a procedure similar to that described by Delavault et al., 2018 where ^{204}Hg beam intensity was calculated based on the measured intensity of the interference free ^{202}Hg beam using the following equation:

$$I_{\text{calculated}}^{204\text{Hg}} = I_{\text{measured}}^{202\text{Hg}} \times \left[\frac{^{204}\text{Hg}}{^{202}\text{Hg}} \right]_{\text{natural}} \times \left(\frac{m_{202\text{Hg}}}{m_{204\text{Hg}}} \right)^{\beta} \quad [1]$$

where β represents the exponential mass bias correction law (Russel et al., 1978) and the natural ratio $^{204}\text{Hg}/^{202}\text{Hg}$ of 0.22988 (Kent, 2008). The interference corrected intensity of the ^{204}Pb ion beam was calculated as follows:

$$I_{\text{calculated}}^{204\text{Pb}} = \left[I^{204\text{Hg} + 204\text{Pb}} \right]_{\text{measured}} - I_{\text{calculated}}^{204\text{Hg}} \quad [2]$$

Typically Pb baseline/blank intensities were on the order of 1800 cps. Following baseline subtraction, the ^{208}Pb counts on NIST612 (38 ppm) and Shap Feldspar (52 ppm) were 345000 cps and 460000 cps respectively, equating to a sensitivity of approximately 9000 cps/ppm. For most analyses the ^{202}Hg counts were very low (1000-3000 cps). However, total $^{204}(\text{Pb}+\text{Hg})$ varied depending on the Pb concentration in each crystal (typically between 3000 and 42000 CPS). To detect analyses with very low signal to noise ratios and potentially large interferences we monitored the $^{204}\text{Hg}/^{204}(\text{Pb}+\text{Hg})$ ratio and removed any analyses where this ratio was greater than 0.15. The median $^{204}\text{Hg}/^{204}(\text{Pb}+\text{Hg})$ ratio across all unknown analyses is 0.03 ± 0.02 (1σ), meaning that intensity of ^{204}Pb beam is on average 20-100x stronger than the ^{204}Hg beam, and therefore easily resolved from the interference. As an extra precaution, analyses with Pb concentrations less than 10 ppm were also excluded to mitigate any additional effects from radiogenic ingrowth in crystals with very low Pb concentration.

Normalisation was carried out using the matrix matched Shap Feldspar with reference values of $^{206}\text{Pb}/^{204}\text{Pb} = 18.271$, $^{207}\text{Pb}/^{204}\text{Pb} = 15.656$, and $^{208}\text{Pb}/^{204}\text{Pb} = 38.258$. Reference materials were analyzed every 15–20 unknowns in a block with NIST 612 glass ($n = 383$ over the 22 sessions). The data were reduced using Iolite 4 with an in-house data reduction scheme that yields Pb isotopic ratios and approximate Pb concentrations. The $^{206}\text{Pb}/^{204}\text{Pb}$, $^{207}\text{Pb}/^{204}\text{Pb}$, and $^{208}\text{Pb}/^{204}\text{Pb}$ ratios of the unknown samples was calculated using standard sample bracketing:

$$\left(\frac{X_{\text{Pb}}}{^{204}\text{Pb}}\right)_{\text{calculated}}^{\text{unknown}} = \frac{\left(\left(\frac{X_{\text{Pb}}}{\frac{I_{\text{measured}}}{^{204}\text{Pb}}}\right)^{\text{unknown}} \times \left[\frac{X_{\text{Pb}}}{^{204}\text{Pb}}\right]_{\text{reference}}^{\text{Shap Kfs}}\right)}{\text{mean} \left(\frac{X_{\text{Pb}}}{\frac{I_{\text{measured}}}{^{204}\text{Pb}}}\right)^{\text{Shap Kfs}}} \quad [3]$$

where X_{Pb} denotes the ^{206}Pb , ^{207}Pb , or ^{208}Pb isotopes and the ‘mean’ refers to the value of a spline interpolated through the measured isotope ratio on the primary standard (Shap Feldspar) at the relevant point in the time series, and is equivalent to the average of the two bracketing standards.

A summary of results for NIST612 during each session is provided in Table DR1. Individual standard analyses are provided in Dataset S1 in the electronic appendix. Means, standard errors, and standard deviations for each sample are reported in Dataset S2 of the electronic appendix. Individual analyses from each of the granites analysed are provided in Dataset S3 of the electronic appendix.

Data Compilation:

In addition to granite orthoclase measurements performed as part of this study we compiled available Pb isotope data on gold and base metal ores from the Yilgarn Craton. Specifically, we focussed on Pb isotope data from Pb-rich sulphides (galena and pyrite) and whole-rock data on magmatic rocks for which initial Pb isotope compositions could be obtained in order to allow direct comparison with feldspar data. The compilation of ore Pb isotope data is provided in Dataset S4 and includes results from Oversby, (1975); Browning et al. (1987), Perring and McNaughton (1990), Barnicoat et al. (1991), McNaughton et al. (1992), McNaughton et al.

(1993), Wang et al. (1993), Gebre-Mariam et al. (1994), Ho et al., (1994), Dalstra et al. (1995), Ojala et al. (1997), Yeats et al. (1998), Qui and McNaughton (1999), Salier (2003), Thorpe (2008), Huston et al. (2014), Huston et al. (2019) and Barrote et al. (2020).

Two-stage Pb Isotope Source Model Age Calculations:

In the Archean changes in $^{206}\text{Pb}/^{204}\text{Pb}$ and $^{207}\text{Pb}/^{204}\text{Pb}$ ratios are highly non-linear with time. Accordingly, it is not always possible to accurately image crustal structure by simply visualising the spatial variations in the initial Pb isotope compositions of Archean rocks of different ages. In the Archean in particular, there can be significant isotopic variability, especially in $^{207}\text{Pb}/^{204}\text{Pb}$, attributed to long-term Pb isotope evolution which is not necessarily related to the fundamental age and/or structure of the crust. To avoid such artefacts in the Pb isotope maps, two-stage bulk silicate earth (BSE) Pb isotope source models ages were calculated from each of the measured Pb isotope ratios following the approach outlined in Hartnady et al., (2022):

$$^{206}\text{Pb}T_{\text{BSE}}^2 = \ln \left[\frac{(\mu_m e^{\lambda_{238}T_0} - \mu_c e^{\lambda_{238}T}) + \left(\left(\frac{^{206}\text{Pb}}{^{204}\text{Pb}} \right)_m^{T_0} - \left(\frac{^{206}\text{Pb}}{^{204}\text{Pb}} \right)_c^T \right)}{(\mu_m - \mu_c)} \right] \cdot (\lambda_{238})^{-1}, \quad [4]$$

$$^{207}\text{Pb}T_{\text{BSE}}^2 = \ln \left[\frac{\left(\frac{\mu_m}{137.818} e^{\lambda_{235}T_0} - \frac{\mu_c}{137.818} e^{\lambda_{235}T} \right) + \left(\left(\frac{^{207}\text{Pb}}{^{204}\text{Pb}} \right)_m^{T_0} - \left(\frac{^{207}\text{Pb}}{^{204}\text{Pb}} \right)_c^T \right)}{\left(\frac{\mu_m - \mu_c}{137.818} \right)} \right] \cdot (\lambda_{235})^{-1}, \quad [5]$$

$$^{208}\text{Pb}T_{\text{BSE}}^2 = \ln \left[\frac{(\mu_m \kappa_m e^{\lambda_{232}T_0} - \mu_c \kappa_c e^{\lambda_{232}T}) + \left(\left(\frac{^{208}\text{Pb}}{^{204}\text{Pb}} \right)_m^{T_0} - \left(\frac{^{208}\text{Pb}}{^{204}\text{Pb}} \right)_c^T \right)}{(\mu_m \kappa_m - \mu_c \kappa_c)} \right] \cdot (\lambda_{232})^{-1}. \quad [6]$$

These equations show that an estimate of the time of extraction of the crustal source from a mantle reference reservoir (T_{Res}) can be obtained given knowledge of the Pb isotope composition at the time of the crystallisation of the granite, and the initial Pb isotope composition and model initiation time (T_0) of a reference reservoir (e.g. depleted mantle or BSE at 4.5 Ga). Here μ_m , μ_s , κ_m and κ_s denote the $^{238}\text{U}/^{204}\text{Pb}$ and $^{232}\text{Th}/^{238}\text{U}$ ratios in the mantle and crustal source reservoirs respectively, λ represents the decay constant for the relevant decay scheme and T denotes the samples crystallisation age.

The equations above are consequent from the linear parameterisation for Pb isotope evolution of Albarede and Juteau, (1984), and are analogous to two-stage depleted mantle model age or ‘crust formation age’ calculations that are commonly applied to zircon Hf isotope data (e.g. Dhuime et al., 2012). Zametzer et al., (2022) recently noted that the Pb isotope composition of granites from the Yilgarn Craton are better reproduced using the global Pb isotope evolution framework of Maltese and Mezger, (2020), as opposed to Stacey and Kramers, (1975) or Cummings and Richards, (1975) which have historically been applied to Archean cratons in Australia and elsewhere. Therefore, for two-stage Pb isotope source model ages and Pb isotope evolution models presented below are calculated in the Maltese and Mezger (2020) reference frame with initial conditions outlined in Table DR3 ($T_0 = 4.498$ Ga, $\mu_c=8.42$, $\kappa=4.05$) and Supplementary Dataset 5. Two-stage Pb isotope source model ages are calculated assuming a

crustal μ value (μ_c) of 12 and κ value (κ_c) of 4.75 (Table DR3) as this reproduces the observed Pb isotope variability of granites and ores (see Pb isotope modelling below, Figure DR18).

Spatial Mapping Methods:

Spatial variations in Pb isotope two-stage source model age data (this study), two-stage depleted mantle Hf and Nd isotope model age data (after Lu et al., 2021a, 2021b), and modelled upper mantle shear-wave velocity distributions (after Kennet et al., 2013) are visualised using interpolated maps. These maps were generated using the Empirical Bayesian Kriging interpolation algorithm in the Geostatistical Analyst modelling toolbox in ArcGIS, using a minimum of 10 nearest neighbours within a sampling radius of 100 km and a smoothing factor of 0.5. Contours were extracted from the interpolated model age maps using the Contour function in the Spatial Analyst toolbox in ArcGIS. Maps showing the spatial variation of zircon Hf isotope two-stage depleted mantle model ages, whole-rock Nd two-stage depleted mantle model ages, two-stage BSE Pb isotope models and mantle shear wave velocity models are presented in Figure 3 in the manuscript. A map showing the locations of samples used to generate the whole-rock Nd isotope maps is presented in Figure DR1 below.

Pb Isotope Evolution Modelling:

The Pb isotope evolution of two hypothetical end-member crustal Pb reservoirs (Crust Model A and Crust Model B) were calculated using two-stage Pb isotope evolution models of the form:

$$\left(\frac{{}^{206}\text{Pb}}{{}^{204}\text{Pb}}\right)_T = \left(\frac{{}^{206}\text{Pb}}{{}^{204}\text{Pb}}\right)_{\text{BSE}, 4.498 \text{ Ga}} + \mu_{\text{BSE}}(e^{\lambda_{238} \times 4.498} - e^{\lambda_{238} \times T_S}) + \mu_c(e^{\lambda_{238} \times T_0} - e^{\lambda_{238} \times T}), \quad [7]$$

$$\left(\frac{{}^{207}\text{Pb}}{{}^{204}\text{Pb}}\right)_T = \left(\frac{{}^{207}\text{Pb}}{{}^{204}\text{Pb}}\right)_{\text{BSE}, 4.498 \text{ Ga}} + \frac{\mu_{\text{BSE}}}{137.818}(e^{\lambda_{235} \times 4.498} - e^{\lambda_{235} \times T_S}) + \frac{\mu_c}{137.818}(e^{\lambda_{235} \times T_0} - e^{\lambda_{235} \times T}), \quad [8]$$

and,

$$\left(\frac{{}^{208}\text{Pb}}{{}^{204}\text{Pb}}\right)_T = \left(\frac{{}^{208}\text{Pb}}{{}^{204}\text{Pb}}\right)_{\text{BSE}, 4.498 \text{ Ga}} + \kappa_{\text{BSE}} \cdot \mu_{\text{BSE}}(e^{\lambda_{232} \times 4.498} - e^{\lambda_{232} \times T_S}) + \kappa_c \cdot \mu_c(e^{\lambda_{232} \times T_0} - e^{\lambda_{232} \times T}) \quad [9]$$

where T_0 denotes the time of extraction of the crustal Pb reservoir out of the mantle/BSE, and μ and κ denote the ${}^{238}\text{U}/{}^{204}\text{Pb}$ and ${}^{232}\text{Th}/{}^{238}\text{U}$ ratios in each reservoir respectively. Decay constants for ${}^{238}\text{U}$, ${}^{235}\text{U}$, and ${}^{232}\text{Th}$ are $\lambda_{238}=0.155125 \text{ Ga}^{-1}$, $\lambda_{235}=0.98485 \text{ Ga}^{-1}$, and $\lambda_{232}=0.049475 \text{ Ga}^{-1}$ respectively, following Jaffrey et al., (1971) and Schoene, (2014). Note that the first two terms on the right-hand side of the equations above yields the composition of the BSE at time T_S , which denote the starting composition (X_0, Y_0, Z_0) for the crustal Pb evolution models

The results of Pb isotope modelling are illustrated using the linear parameterisation of Albarede and Juteau, (1984) (Figure DR17), and using conventional Pb isotope evolution diagrams (Figures DR18). The Pb isotope evolution model for Crust Model A assumes the crustal precursor separated from the mantle at 3.3 Ga and was instantaneously fractionated to μ of 12 and κ of 4.75. Crust Model B makes identical assumptions for μ and κ but separates from the mantle at 3.8 Ga. Both models can reproduce the ${}^{208}\text{Pb}/{}^{204}\text{Pb}$ and ${}^{206}\text{Pb}/{}^{204}\text{Pb}$ compositions of the Yilgarn high ${}^{208}\text{Pb}/{}^{204}\text{Pb}$ granites, indicating these granites were contaminated by material from high- μ Paleoarchean crust with fractionated ${}^{232}\text{Th}/{}^{238}\text{U}$ ratios (κ), consistent with the empirical observation that these granites are co-located in regions with Paleoarchean Hf and

Nd isotope model ages. Given that sulphides hosted in high-grade gneiss at Griffin's Find Au deposits have similar Pb isotope compositions this crustal Pb reservoir is interpreted to reflect deeply buried Paleoarchean granulites, which have experienced prior partial melting and melt loss in the presence of residual monazite (e.g. Yakymchuk and Brown, 2019). Only the Crust Model B (3.8 Ga crust) is able to evolve to $^{207}\text{Pb}/^{204}\text{Pb}$ ratios similar to those observed in the Norseman gold ores. This modelling indicates these gold ores, and nearby granites, must have sourced crust of similar age and μ (~ 12). Alternatively, younger crust could evolve to these values but requires $\mu > 12$. However, Crust Model B cannot reproduce the $^{208}\text{Pb}/^{204}\text{Pb}$ ratios for these ores and granites, indicating they formed from ancient high- μ crust with mantle-like κ value (~ 4.0). It is important to note that these models are not intended to model the true Pb isotope evolution but rather the end-member cases, presenting lower and upper bounds and the time of crust formation and granulite facies metamorphism. The true Pb isotope evolution is likely to be approximated by some combination of these two cases.

Estimating Crustal μ , Ω , and κ values

The time-integrated Th/U ratios of a crustal rocks are typically calculated from the measured Pb isotopic compositions as follows (Allègre et al., 1986; Wipperfurth et al., 2018):

$$\kappa_{\text{Pb}} = \frac{\frac{^{208}\text{Pb}^*}{^{206}\text{Pb}^*} \times (e^{\lambda_{238}T_0} - 1)}{(e^{\lambda_{232}T_0} - 1)} \quad [10]$$

where,

$$\frac{^{208}\text{Pb}^*}{^{206}\text{Pb}^*} = \frac{\left(\frac{^{208}\text{Pb}^*}{^{204}\text{Pb}}\right)_m - \left(\frac{^{208}\text{Pb}^*}{^{204}\text{Pb}}\right)_i}{\left(\frac{^{206}\text{Pb}^*}{^{204}\text{Pb}}\right)_m - \left(\frac{^{206}\text{Pb}^*}{^{204}\text{Pb}}\right)_i} \quad [11]$$

Here, the subscripts “ m ” and “ i ” represent the measured lead isotope ratios of the sample and initial Pb isotope composition of the rocks source. First, a corrected lead composition, referred to as the “radiogenic lead ratio” $^{208}\text{Pb}^*/^{204}\text{Pb}$ is calculated. Assuming a closed system, the development of the radiogenic lead ratios only depends on time and the Th/Pb and U/Pb ratios, allowing calculations of time-integrated κ_{Pb} .

Many studies use the composition of Pb in Canyon Diablo Troilite with $^{208}\text{Pb}/^{204}\text{Pb} = 29.476$ and $^{206}\text{Pb}/^{204}\text{Pb} = 9.307$ as an initial source composition (Wipperfurth et al., 2018; Tatsumoto et al., 1973; Blichert-Toft et al., 2010), where T is the age of the Earth (taken to be 4.568 Ga), and λ_x denotes the relevant decay constants. However, doing so assumes a single stage closed system Pb isotope evolution from primordial Pb compositions. Although to a first order this model provides a reasonable approximation for the Pb isotope evolution of mantle-derived rocks, it does not distinguish between mantle and crustal Pb isotope evolution, and will therefore systematically underestimate Th/U ratios for rocks with long crustal residence times; such as granites formed by reworking old pre-existing crust. Moreover, evidence from other long-lived radiogenic isotope systems (Sm–Nd, Lu–Hf and Re–Os) indicates that both crust extraction and mantle depletion occurred episodically and may have varied substantially over geological time (Kemp et al., 2006; Pearson et al., 2007). In order to obtain more accurate estimates of crustal Th/U ratios from Pb isotope data one must therefore take into account the time at which different portions of the continental crust separated from the mantle.

We estimating crustal U/Pb, Th/Pb, and Th/U ratios that combines initial Pb isotope data with knowledge of 'crust formation ages', such as those obtained from zircon Hf isotope data or whole-rock Sm-Nd isotope data. To account for variable mantle and crustal residence times, we model Pb isotope evolution using a two-stage evolution as shown in the previous section. The first two terms on the right hand side of the equations above reflect Pb isotopic evolution in the mantle prior to crust extractions at time T_s , whereas the last term on the right reflects radiogenic Pb production within the continental crust between the time of its initial extraction from the mantle (T_s) and time of subsequent reworking to form the granite (T). Note that as T approaches T_s the term describing the crustal Pb isotope evolution approaches 0. If the mantle Pb isotope evolution is known one can substitute the first two terms for the Pb isotopic composition of the mantle at the time of crust formation, and simplify the expressions above to calculate crustal U/Pb (μ_c) and Th/Pb (Ω_c) ratios (and hence Th/U ratios) such that:

$$\mu_c = \frac{\left(\frac{^{206}\text{Pb}}{^{204}\text{Pb}}\right)_T - \left(\frac{^{206}\text{Pb}}{^{204}\text{Pb}}\right)_{T_s}^{mantle}}{(e^{\lambda_{238}T} - e^{\lambda_{238}T_s})} \quad [12]$$

Or,

$$\mu_c = 137.88 \times \frac{\left(\frac{^{207}\text{Pb}}{^{204}\text{Pb}}\right)_T - \left(\frac{^{207}\text{Pb}}{^{204}\text{Pb}}\right)_{T_s}^{mantle}}{(e^{\lambda_{235}T} - e^{\lambda_{235}T_s})} \quad [13]$$

And,

$$\Omega_c = \frac{\left(\frac{^{208}\text{Pb}}{^{204}\text{Pb}}\right)_T - \left(\frac{^{208}\text{Pb}}{^{204}\text{Pb}}\right)_{T_s}^{mantle}}{(e^{\lambda_{238}T} - e^{\lambda_{238}T_s})} \quad [14]$$

μ , Ω , and κ values calculated using this two-stage approach are provided in Dataset-DR6 of the electronic appendix.

References

- Albarede, F., and Juteau, M. 1984. Unscrambling the lead model ages. *Geochimica et Cosmochimica Acta*, v. 48, no. 1, p. 207–212.
- Allègre, C. J., Dupré, B., and Lewin, E. 1986. Thorium/uranium ratio of the Earth. *Chemical Geology*, v. 56, no. 3-4, p. 219–227.
- Barnicoat, A. C., Fare, R. J., Groves, D. I., and McNaughton, N. J., 1991, Syn-metamorphic lode-gold deposits in high-grade Archean settings: *Geology*, v. 19, no. 9, p. 921–924.
- Barrote, V.R., Tessalina, S., McNaughton, N., Jourdan, F., Hollis, S.P., Ware, B., Zi, J-W. 2020. 4D history of the Nimbus VHMS ore deposit in the Yilgarn Craton, Western Australia. *Precambrian Research*, v. 337, p. 105536.
- Blichert-Toft, J., Zanda, B., Ebel, D.S. and Albarède, F., 2010. The solar system primordial lead. *Earth and Planetary Science Letters*, v. 300, no. 1-2, p.152–163.
- Browning, P., Groves, D. I., Blockley, J., and Rosman, K., 1987, Lead isotope constraints on the age and source of gold mineralization in the Archean Yilgarn Block, Western Australia: *Economic Geology*, v. 82, no. 4, p. 971–986.
- Cumming, G.L., and Richards, J.R. 1975. Ore lead isotope ratios in a continuously changing Earth. *Earth and Planetary Science Letters*, v. 28, no. 2, p. 155–171.
- Dalstra, H.J., 1995. Metamorphic and structural evolution of greenstone belts of the Southern Cross - Diemals region of the Yilgarn Block, Western Australia, and its relationship to gold mineralisation. PhD thesis (unpublished), University of Western Australia.
- Delavault, H., Dhuime, B., Hawkesworth, C., and Marschall, H. R., 2018, Laser-ablation MC-ICP-MS lead isotope microanalysis down to 10 µm: application to K-feldspar inclusions within zircon: *Journal of Analytical Atomic Spectrometry*, v. 33, no. 2, p. 195–204.
- Dhuime, B., Hawkesworth, C. J., Cawood, P. A., and Storey, C. D. 2012. A change in the geodynamics of continental growth 3 billion years ago. *Science*, v. 335, no. 6074, 1334–1336.
- Gebre-Mariam, M., Groves, D.I., McNaughton, N.J., Mikucki, E.J., Vearncombe, J.R., 1993. Archaean Au-Ag mineralisation at Racetrack, near Kalgoorlie, Western Australia: a high crustal-level expression of the Archaean composite lode-gold system. *Mineralium Deposita* v. 28, no. , p. 375–387
- Hartnady, M.I.H, Kirkland, C.L., Smithies, R.H., Johnson, S. P., & Johnson, T.E. 2022. Pb isotope insight into the formation of the Earth's first stable continents. *Earth and Planetary Science Letters*, v. 578, p. 117319.
- Ho, S. E., McNaughton, N. J., and Groves, D. I., 1994, Criteria for determining initial lead isotopic compositions of pyrite in Archaean lode-gold deposits: a case study at Victory, Kambalda, Western Australia: *Chemical Geology*, v. 111, no. 1-4, p. 57-84.

Huston, D.L., Champion, D.C., Cassidy, K.F., 2014. Tectonic controls on the endowment of Neoproterozoic cratons in volcanic-hosted massive sulfide deposits: evidence from lead and neodymium isotopes. *Economic Geology* v. 109, no. 1, p. 11–26.

Huston, D.L., Champion, D.C., Ware, B., Carr, G., Maas, R., Tassalana, S., 2019. Preliminary national-scale lead isotope maps of Australia. *Geoscience Australia. Record* 2019/001.

Jaffey, A.H., Flynn, K.F., Glendenin, L.E., Bentley, W.T., and Essling, A.M. 1971. Precision measurement of half-lives and specific activities of U 235 and U 238. *Physical Review C*, v. 4, no. 5, p.1889–1906.

Kemp, A.I.S., Hawkesworth, C.J., Paterson, B.A. and Kinny, P.D., 2006. Episodic growth of the Gondwana supercontinent from hafnium and oxygen isotopes in zircon. *Nature*, v. 439, no. 7076, p. 580–583.

Kennett, B. L., Fichtner, A., Fishwick, S., and Yoshizawa, K. 2013. Australian seismological reference model (AuSREM): mantle component. *Geophysical Journal International*, v. 192, no. 2, 871–887.

Kent, A. J., 2008, In-situ analysis of Pb isotope ratios using laser ablation MC-ICP-MS: Controls on precision and accuracy and comparison between Faraday cup and ion counting systems: *Journal of Analytical Atomic Spectrometry*, v. 23, no. 7, p. 968–975.

Liebmann, J., Ware, B., Hartnady, M.I., Kirkland, C.L., Timms, N.E. and Evans, N.J. 2023. Albany K-Feldspar: A New Pb Isotope Reference Material. *Geostandards and Geoanalytical Research*.

Lu, Y., Wingate, M.T.D., Champion, D.C., Smithies, R.H., Johnson, S.P., Mole, D.R., Poujol, M., Zhao, J., Maas, R. and Creaser, R.A., 2021a. Samarium–Neodymium isotope map of Western Australia: Geological Survey of Western Australia, digital data layer, <www.dmirs.wa.gov.au/geoview>.

Lu, Y., Wingate, M.T.D., Romano, S.S., Mole, D.R., Kirkland, C.L., Kemp, A.I.S., Belousova, E.A., Smithies, R.H., Gessner, K. and Johnson, S.P. 2021b, Zircon lutetium–hafnium isotope map of Western Australia: Geological Survey of Western Australia, digital data layer, <www.dmirs.wa.gov.au/geoview>.

Maltese, A., and Mezger, K. 2020. The Pb isotope evolution of bulk silicate earth: Constraints from its accretion and early differentiation history. *Geochimica et Cosmochimica Acta*, v. 271, p. 179–193.

McNaughton, N.J. Cassidy, K.F., Dahl, N., De Laeter, J.R., Golding, S.D., Groves, D.I., Ho, S.E., Mueller, A.G., Perring, C.S., Sang, J.H., 1992. The source of ore components in lode-gold deposits of the Yilgarn Block, Western Australia. *Geology Department and University Extension, University of Western Australia Publication* v. 22, p. 351–363

McNaughton, N.J., Compston, W., Barley, M.E., 1993. Constraints on the age of the Warrawoona Group, eastern Pilbara Block, Western Australia. *Precambrian Research*, v. 60, no. 1-4, p. 69–98.

- Ojala, V.J., McNaughton, N.J., Groves, D.I., Ridley, J.R., Fanning, C.M., 1997. The Archaean Granny Smith gold deposit, Western Australia: age and Pb-isotope tracer studies. *Chronique de la Recherche Minière*, p. 75–89.
- Oversby, V.M., 1975, :Lead isotopic systematics and ages of Archaean acid intrusives in the Kalgoorlie-Norseman area, Western Australia, *Geochimica et Cosmochimica Acta*, v. 39, no. 8, p. 1107-1125.
- Paul, B., Woodhead, J. D., and Hergt, J., 2005, Improved in situ isotope analysis of low-Pb materials using LA-MC-ICP-MS with parallel ion counter and Faraday detection: *Journal of Analytical Atomic Spectrometry*, v. 20, no. 12, p. 1350–1357.
- Pearson, D.G., Parman, S.W. and Nowell, G.M., 2007. A link between large mantle melting events and continent growth seen in osmium isotopes. *Nature*, v. 449, no. 7159, p. 202–205.
- Perring, C., and McNaughton, N., 1990, Proterozoic remobilization of ore metals within Archaean gold deposits: Lead isotope evidence from Norseman, Western Australia.
- Qiu, Y.M., McNaughton, N.J., 1999. Source of Pb in orogenic lode-gold mineralisation: Pb isotope constraints from deep crustal rocks from the southwestern Archaean Yilgarn Craton, Australia. *Mineralium Deposita* v. 34, no. 4, p. 366–381.
- Russell, W., Papanastassiou, D., and Tombrello, T., 1978, Ca isotope fractionation on the Earth and other solar system materials: *Geochimica et Cosmochimica Acta*, v. 42, no. 8, p. 1075–1090.
- Salier, B.P., 2003. The timing and source of gold-bearing fluids in the Laverton Greenstone Belt, Yilgarn Craton, with emphasis on the Wallaby gold deposit. PhD Thesis, University of Western Australia , p. 379
- Schoene, B. 2014. 4.10-U–Th–Pb Geochronology. *Treatise on geochemistry*, Chapter 4, p. 341–378.
- Stacey, J.S., and Kramers, J.D. 1975. Approximation of terrestrial lead isotope evolution by a two-stage model. *Earth and Planetary Science Letters*, v. 26, no. 2, 207–221.
- Tatsumoto, M., Knight, R.J. and Allegre, C.J., 1973. Time differences in the formation of meteorites as determined from the ratio of lead-207 to lead-206. *Science*, v. 180, no. 4092, p. 1279–1283.
- Thorpe, R.I., 2008. Release of lead isotope data in 4 databases: Canadian, Western Superior, foreign, and whole rock and feldspar. *Geological Survey of Canada Open File 5664*.
- Wang, L.G., McNaughton, N.J., Groves, D.I., 1993. An overview of the relationship between granitoid intrusions and gold mineralisation in the Archaean Murchison Province, Western Australia. *Mineralium Deposita* v. 28, no. 6, p. 482–494.
- Wipperfurth, S.A., Guo, M., Šrámek, O. and McDonough, W.F., 2018. Earth's chondritic Th/U: Negligible fractionation during accretion, core formation, and crust–mantle differentiation. *Earth and Planetary Science Letters*, v. 498, p.196–202.

Woodhead, J. D., and Hergt, J. M., 2001, Strontium, neodymium and lead isotope analyses of NIST glass certified reference materials: SRM 610, 612, 614: *Geostandards Newsletter*, v. 25, no. 2–3, p. 261–266.

Yakymchuk, C., and Brown, M. 2019. Divergent behaviour of Th and U during anatexis: Implications for the thermal evolution of orogenic crust. *Journal of Metamorphic Geology*, v. 37, no. 7, 899–916.

Yeats, C.J., Groves, D.I., 1998. The Archaean Mount Gibson gold deposits, Yilgarn Craton, Western Australia: Products of combined synvolcanic and syntectonic alteration and mineralisation. *Ore Geology Reviews* v. 13, no. 1–5, p. 103–129

Zametzer, A., Kirkland, C.L., Hartnady, M.I.H, Barham, M., Champion, D.C., Bodorkos, S., Smithies, R.H. and Johnson, S. P. (2022). Applications of Pb isotopes in granite K-feldspar and Pb evolution in the Yilgarn Craton. *Geochimica et Cosmochimica Acta*, v. 320, 279–303.

Table DR1. Summary of Pb isotope results for NIST612 glass for all analytical sessions.

Session	Detectors	Date	Standard	$^{206}\text{Pb}/^{204}\text{Pb}$	$^{207}\text{Pb}/^{204}\text{Pb}$	$^{208}\text{Pb}/^{204}\text{Pb}$	Samples Analysed
1	FC-IC	16/6/20	NIST612 Glass	17.106 ± 0.028	15.513 ± 0.023	36.984 ± 0.053	142810; 142919; 178199; 182454; 185933; 185985; 198213; 198220; 199024; 199047; 204585
2	FC-IC	17/6/20	NIST612 Glass	17.093 ± 0.033	15.508 ± 0.024	36.968 ± 0.076	155522; 178054; 178058; 198212; 199023; 199046
3	FC-IC	30/7/20	NIST612 Glass	17.104 ± 0.024	15.511 ± 0.020	36.989 ± 0.033	155513; 155822; 168902; 185992
4	FC-IC	31/7/20	NIST612 Glass	17.100 ± 0.013	15.508 ± 0.013	36.984 ± 0.022	179449; 185992
5	FC-IC	3/8/20	NIST612 Glass	17.094 ± 0.0034	15.515 ± 0.033	37.016 ± 0.102	155502
6	FC-IC	4/8/20	NIST612 Glass	17.093 ± 0.0030	15.514 ± 0.028	36.988 ± 0.063	104964; 155511; 168974; 169068; 178059; 182603; 98260
7	FC-IC	5/8/20	NIST612 Glass	17.091 ± 0.016	15.498 ± 0.016	36.942 ± 0.037	142920; 185986; 185929; 185997; 192226; 193316; 207529
8	FC-IC	8/9/20	NIST612 Glass	17.113 ± 0.040	15.515 ± 0.040	36.988 ± 0.080	155503; 155507; 155514; 168970; 169096; 178052; 178057; 178122; 178194; 182316; 182379
9	FC-IC	9/9/20	NIST612 Glass	17.114 ± 0.042	15.514 ± 0.036	36.980 ± 0.054	168903; 199034; 207503; 207505; 207525; 207526
10	FC-IC	10/9/20	NIST612 Glass	17.111 ± 0.034	15.525 ± 0.034	37.012 ± 0.075	142815; 142994; 155504; 168901; 168956; 178190; 178196

Session	Detectors	Date	Standard	$^{206}\text{Pb}/^{204}\text{Pb}$	$^{207}\text{Pb}/^{204}\text{Pb}$	$^{208}\text{Pb}/^{204}\text{Pb}$	Samples Analysed
11	FC-IC	14/9/20	NIST612 Glass	17.100 ± 0.037	15.507 ± 0.025	36.999 ± 0.051	182783; 183149; 207524; 207530; 207630
12	FC-IC	2/11/20	NIST612 Glass	17.101 ± 0.026	15.508 ± 0.029	36.972 ± 0.054	142813; 155505; 155879; 168963; 168966
13	FC-IC	16/11/20	NIST612 Glass	17.088 ± 0.029	15.510 ± 0.029	37.001 ± 0.060	179669; 193433; 182308; 199049; 199700; 207527; 207528; 211059; 214243
14	FC-IC	19/4/21	NIST612 Glass	17.096 ± 0.020	15.510 ± 0.018	37.003 ± 0.043	155843; 155874; 155875; 205935; 205942; 219311; 219901; 224305
15	FC-IC	20/4/21	NIST612 Glass	17.093 ± 0.016	15.495 ± 0.016	36.946 ± 0.036	219902; 224316; 224332; 224329; 224339; 224378; 224380; 224395
16	IC	03/05/2022	NIST612 Glass (16 μm)	17.104 ± 0.151	15.513 ± 0.168	37.066 ± 0.375	ARC-1A; ARC-19; ARC-20; ARC-21; ARC-22; ARC-23; ARC-24; ARC-30; ARC-31
17	IC	27/06/2022	NIST612 Glass	17.098 ± 0.071	15.508 ± 0.064	37.013 ± 0.168	224345; 224351; 224357; 242405; ARC-85
18	IC	06/07/2022	NIST612 Glass	17.102 ± 0.034	15.485 ± 0.034	37.090 ± 0.074	227403
19	IC	15/08/2022	NIST612 Glass	17.094 ± 0.152	15.524 ± 0.144	37.045 ± 0.376	ARC-86; ARC-87; ARC-88; ARC-89; ARC-90; ARC-96; ARC-97; ARC-99; ARC-100;
20	IC	16/08/2022	NIST612 Glass	17.093 ± 0.039	15.508 ± 0.037	37.038 ± 0.087	ARC-101; ARC-104; ARC-118; ARC-119; ARC-40; ARC-45; ARC-48; ARC-58; ARC-67; ARC-68; ARC-69; ARC-70
21	IC	17/08/2022	NIST612 Glass	17.076 ± 0.055	15.476 ± 0.053	36.963 ± 0.117	ARC-71; ARC-74; ARC-75; ARC-76; ARC-77; ARC-78; ARC-79; ARC-80; ARC-81; ARC-82; ARC-83;
22	IC	02/11/2022	NIST612 Glass	17.081 ± 0.056	15.497 ± 0.049	36.981 ± 0.106	ARC-32; ARC-33; ARC-34; ARC-35; ARC-36; ARC-37; ARC-38;

Table DR3 - Parameters used for Pb isotope modelling.

Pb Reservoir	X₀	Y₀	Z₀	T₀ (Ga)	μ	κ
BSE Model ^a	9.345	10.37	29.51	4.498	8.42	4.05
Crust Model A	12.214	13.921	31.921	3.300	12	4.75
Crust Mode B	11.081	12.919	30.956	3.800	12	4.75

^a*Bulk Silicate Earth (BSE) model parameters after Maltese and Mezger, 2020. Initial Pb isotope compositions (X₀, Y₀, and Z₀) for the crustal Pb reservoirs are derived from the BSE model at the time of separation of the crust (T₀).*

Supplementary Figures

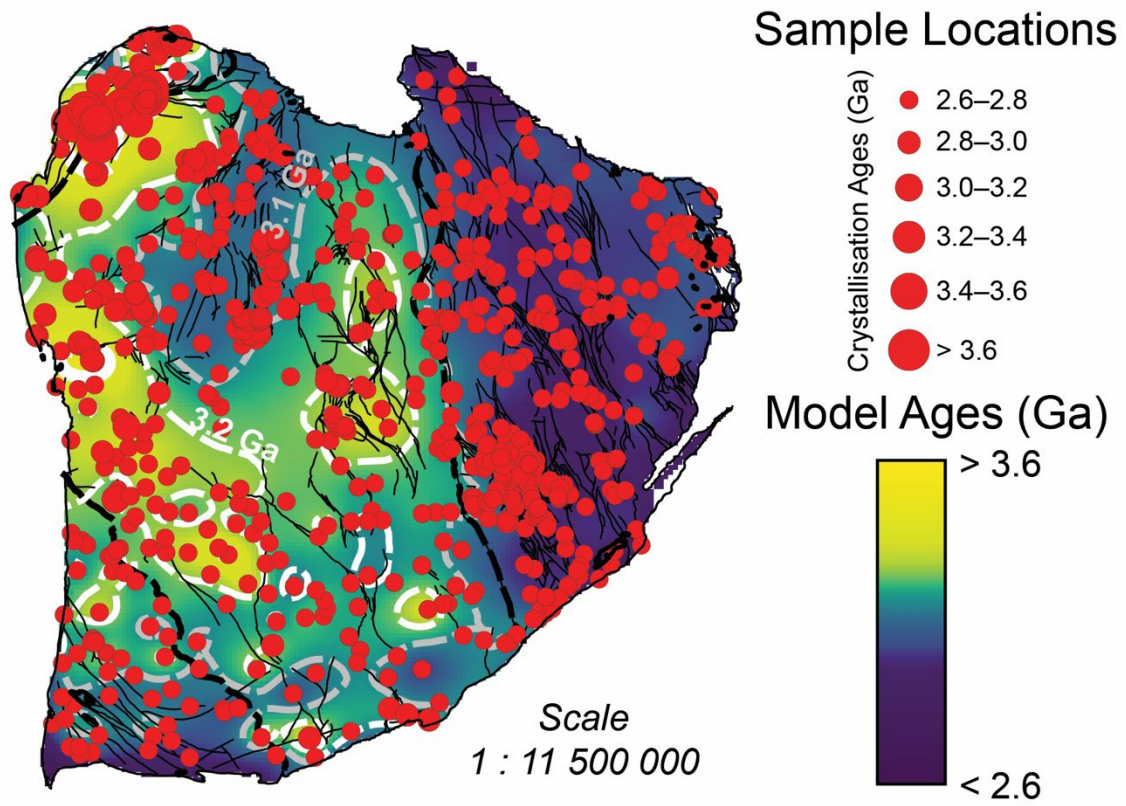


Figure DR1. Interpolated maps of whole-rock Nd isotope two-stage depleted mantle model ages (data from Lu et al., 2021a), showing the spatial variation in estimated age of the crust across the Yilgarn Craton. Contours enclose regions of crust with model ages older than 3.1Ga and 3.2 Ga.

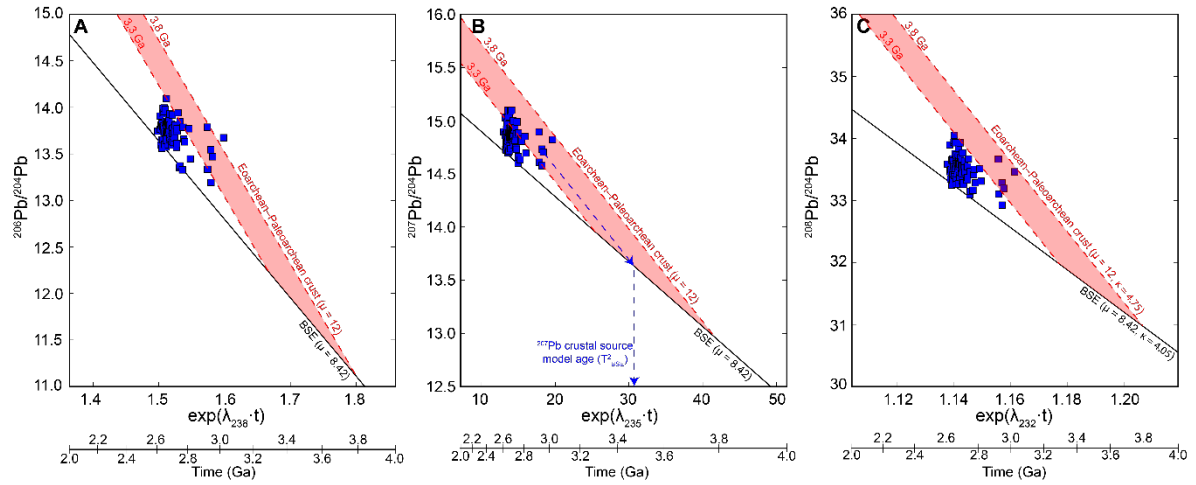


Figure DR2. Linear Pb isotope evolution diagrams following Albarede and Juteau (1984) showing Pb isotope evolution model for the bulk silicate earth (BSE) after Maltese and Mezger (2020) (black line), Pb isotope composition of granites from the Yilgarn Craton (blue squares) and the Pb isotope evolution array for an Eoarchean–Paleoarchean crustal Pb reservoir with $\mu = 12$ and $\kappa = 4.75$ (red shaded region). Note that the scatter defined by the granite Pb isotope data are consistent with mixing between a mantle-derived Pb reservoir and high- μ , high- κ Eoarchean–Paleoarchean crustal Pb reservoir. Dashed blue arrows depict the projection used to calculate two-stage Pb source model ages.

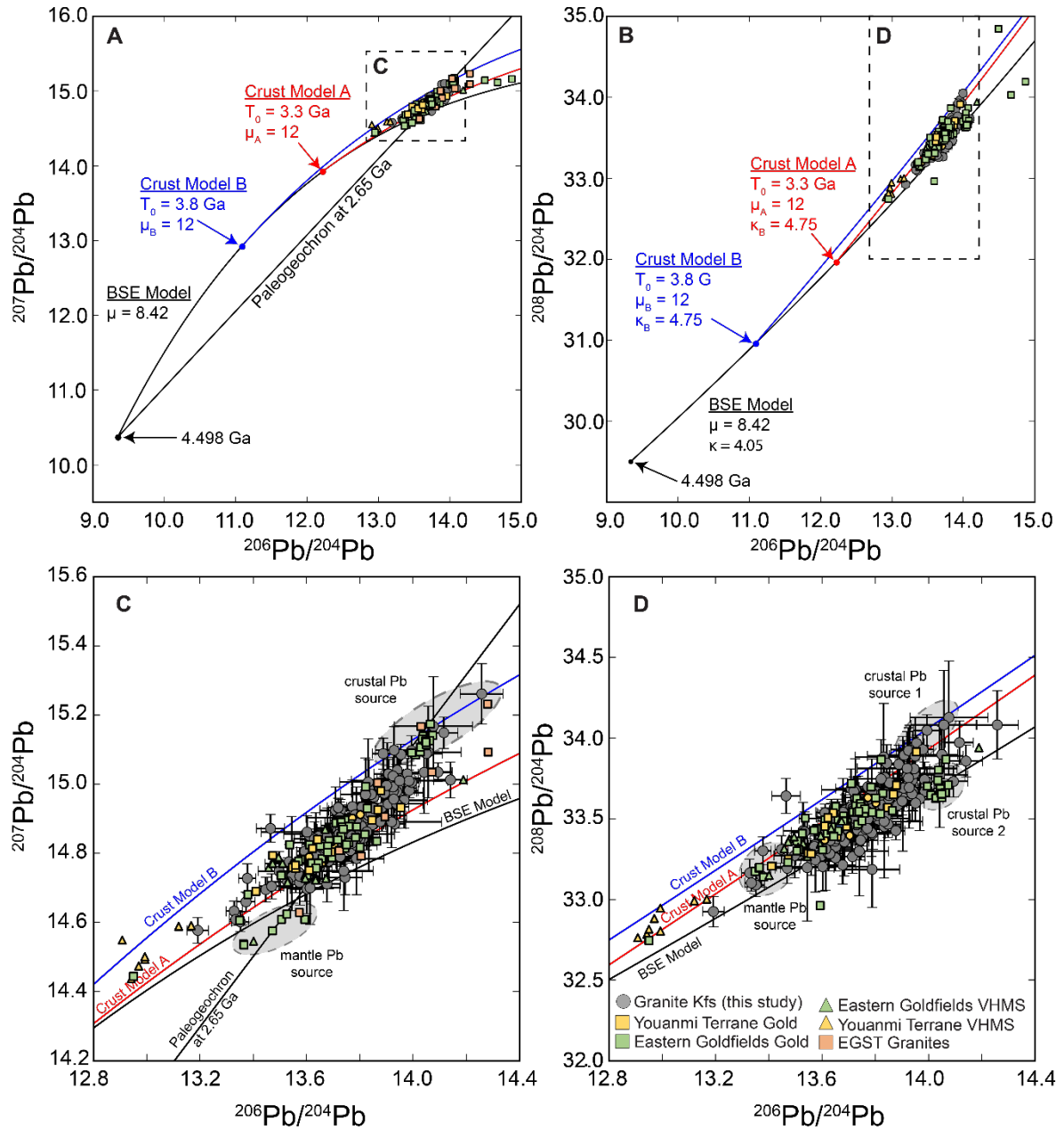


Figure DR3. Pb isotope evolution diagrams showing the initial Pb isotope compositions of granites and ores from the Yilgarn Craton, along with Pb isotope evolution models for the bulk silicate earth (BSE) after Maltese and Mezger (2020), and two hypothetical crustal Pb reservoirs extracted out of the BSE at 3.3 Ga (Model A, red curve) and 3.8 Ga (Model B, blue curve), with $\mu = 12$ and $\kappa = 4.75$. Note that the Pb isotope data for both granites and ores can be explained by mixing between a mantle Pb reservoir and two distinct Eoarchean–Paleoarchean crustal Pb reservoirs; one with fractionated $^{232}\text{Th}/^{238}\text{U}$ ($\kappa \sim 4.7\text{--}4.8$) and one with unfractionated mantle-like $^{232}\text{Th}/^{238}\text{U}$ ($\kappa \sim 4.0$). Error bars denote 1σ uncertainties.